Nonlinear Analysis of MEMS Electrostatic Microactuators: Primary and Secondary Resonances of the First Mode*

F. Najar, A.H. Nayfeh, E.M. Abdel-Rahman, S. Choura and S. El-Borgi

Journal of Vibration and Control 2010 16: 1321 originally published online 15 April 2010

DOI: 10.1177/1077546309106520

Nonlinear Analysis of MEMS Electrostatic Microactuators: Primary and Secondary Resonances of the First Mode*

F. NAJAR
Applied Mechanics and Systems Research Laboratory, Tunisia Polytechnic School, BP 743, La Marsa 2078, Tunisia

A. H. NAYFEH
Department of Engineering Science and Mechanics, MC 0219, Virginia Polytechnic Institute and State University, Blacksburg, VA 24061, USA

E. M. ABDEL-RAHMAN
Department of Systems Design Engineering, University of Waterloo, Waterloo, Ontario, Canada N2L 3G1 (eihab@engmail.uwaterloo.ca)

S. CHOURA
S. EL-BORGI
Applied Mechanics and Systems Research Laboratory, Tunisia Polytechnic School, BP 743, La Marsa 2078, Tunisia

(Received 29 July 2008; accepted 23 February 2009)

Abstract: We use a discretization technique that combines the differential quadrature method (DQM) and the finite difference method (FDM) for the space and time, respectively, to study the dynamic behavior of a microbeam-based electrostatic microactuator. The adopted mathematical model based on the Euler–Bernoulli beam theory accounts for the system nonlinearities due to mid-plane stretching and electrostatic force. The nonlinear algebraic system obtained by the DQM–FDM is used to investigate the limit-cycle solutions of the microactuator. The stability of these solutions is ascertained using Floquet theory and/or long-time integration. The method is applied for large excitation amplitudes and large quality factors for primary and secondary resonances of the first mode in case of hardening-type and softening-type behaviors. We show that the combined DQM–FDM technique improves convergence of the dynamic solutions. We identify primary, subharmonic, and superharmonic resonances of the microactuator. We observe the occurrence of dynamic pull-in due to subharmonic and superharmonic resonances as the excitation amplitude is increased. Simultaneous resonances of the first and higher modes are identified for large orbits in both primary and secondary resonances.

Key words: Microelectromechanical systems, microactuator, differential quadrature method, finite difference method, secondary resonance, simultaneous resonance.

* This paper was contributed by Professor Guiseppe Rega

Journal of Vibration and Control, **16(9):** 1321–1349, 2010 DOI: 10.1177/1077546309106520

Figures 2–25 appear in color online: http://jvc.sagepub.com

1. INTRODUCTION

The classical modeling and design processes are no longer efficient for the rapidly growing microelectromechanical system (MEMS) market. In fact, the need for new technologies requires the use of innovative processes for the purpose of minimizing the necessary time to bring a system from the design phase to full-scale production (*time-to-market*). New modeling and design processes aim at generating reduced-order models (ROMs) that integrate multiple physics domains. Most of the developed models are ROMs that emphasize integration of the mechanical device into the system model using lumped models such as rigid-body approximations (Mukherjee et al., 2000) and equivalent circuit simulations (Veijola et al., 1998). The integration of a black-box ROM into the chip macromodel permits simulations at the system level. The accuracy of these simulations plays a major role in reducing the time-to-market. Nevertheless, newly developed ROMs have not yet been met with the full satisfaction of the MEMS industry.

Recently reported ROMs successfully simulated the dynamics of microstructures, including geometric and electrostatic nonlinearities (De and Aluru, 2006; Najar et al., 2006; Nayfeh et al., 2007). Two different approaches can be found in the literature to approximating accurately the behavior of microstructures. For simple and relatively complex geometry, the partial differential equations (PDEs) describing the microactuator motions are directly solved using semi-analytical methods that lead to a reduced number of ordinary differential equations (ODEs) by approximating the space variables or its derivatives using linear combinations of basis functions (Najar et al., 2006; Nayfeh et al., 2007). For complex geometry, the space domain is discretized and the original PDEs are transformed into a very large time-dependent system (Zook et al., 1992). This latter approach is not suitable for dynamic analysis even if efficient size-reduction techniques, such as the proper orthogonal decomposition (POD) (Mehner et al., 2000), are applied.

The selection of the discretization method is a major key to determining the number of resulting ODEs. Lumped models are time efficient and can be successfully used to solve the dynamics of systems subject to simple excitations with very small displacements about a given equilibrium point (Shkel, 2006). On the other hand, it was demonstrated that the integration of system nonlinearities is a prerequisite for accurate approximation of the microsystem behavior (Younis, 2001; Chao et al., 2006; Nayfeh et al., 2007). Finite element method (FEM) discretization of MEMS devices, incorporating complex geometry, using commercial software can produce more accurate results. However, this discretization remains a cumbersome phase in the design process, even when using automated size-reduction routines. Moreover, the dynamic behavior cannot be fully examined using these models. On the other hand, there are other discretization techniques, such as differential quadrature method (DQM), that approximate the original system by a small number of ODEs. These techniques preserve the complexity of the system response, due to nonlinearities, in a parameterized model that is well suited to relatively complex geometries. It was first used by Kuang and Chen (2004) and Najar et al. (2005, 2006) to solve the nonlinear PDE of a variable-geometry microactuator. With this technique, the microsystem dynamics can be accurately simulated using fewer degrees of freedom.

In the present study, we employ a mathematical model, which accounts for the nonlinearities due to mid-plane stretching and electrostatic forcing, to examine the dynamic behavior of a clamped–clamped microbeam-based electrostatic microactuator. A technique combining

the DQM and the finite difference method (FDM) is developed and implemented to discretize the space and time derivatives of the microactuator, which is used in turn to investigate its nonlinear behavior. This study aims at providing a better understanding of the behavior of microactuators and, thus, identification of their advantages and limitations. Moreover, as discussed earlier, the nonlinear phenomena observed in the responses of microactuators can be used to improve their performance. They include (a) increase of the signal-to-crosstalk ratio for microresonators using superharmonic resonances (De and Aluru, 2006), (b) introduction of superharmonic excitations to control the dynamic pull-in in microactuators (Lenci and Rega, 2006), and (c) design of low-voltage microswitches using dynamic pull-in (Nayfeh et al., 2007).

Unlike other discretization methods, such as FEM, that require large computation times, the DQM–FDM technique simulates periodic motions (limit-cycle solutions) in much shorter times. Moreover, the computed solutions are accurate for both small and large orbits. In fact, as pointed out in earlier studies, the approximation of the forcing term by a Taylor-series expansion leads to erroneous results for large-amplitude orbits (Chao et al., 2006; Najar et al., 2006; Nayfeh et al., 2007). The DQM–FDM technique does not require such an approximation. Further, unlike perturbation techniques and other analytical methods (Nayfeh and Younis, 2005), the present technique does not require additional effort to extend the analysis from primary to secondary resonances. In this study, we investigate the basic dynamics of the microactuator and compare its results with recently reported models. We then examine primary and secondary resonances and bifurcations of the microactuator hardening-type and softening-type responses over a wide frequency range and small- and large-amplitude excitations.

2. PROBLEM FORMULATION

We adopt a fixed–fixed silicon microbeam for analyzing the static and dynamic behaviors of MEMS-based electrostatic microactuators, shown in Figure 1. The microactuator is actuated by a combination of DC and AC voltages. The static deflection, due to the application of the DC voltage alone, is commonly taken as a reference configuration about which the microbeam oscillates in the presence of an AC voltage. Hence, it is necessary to determine first the static deflection and then examine the dynamic behavior. The geometric and material properties of the microactuator, shown in Figure 1, are listed in Table 1.

The microbeam dynamics is described by the following integral–partial–differential equation and associated boundary conditions (Younis et al., 2003):

$$\rho A\ddot{\tilde{w}} + \hat{c}\dot{\tilde{w}} + E_f I\tilde{w}^{iv} = \frac{1}{2}\varepsilon b\frac{\left[V_p + \tilde{v}(\tilde{t})\right]^2}{(d-\tilde{w})^2} + \left[\frac{E_f A}{2l}\int_0^l \tilde{w}'^2\, d\tilde{x} + \tilde{N}\right]\tilde{w}'', \tag{1}$$

$$\tilde{w}(0,\tilde{t}) = \tilde{w}(l,\tilde{t}) = 0 \quad \text{and} \quad \tilde{w}'(0,\tilde{t}) = \tilde{w}'(l,\tilde{t}) = 0, \tag{2}$$

where the transverse deflection is denoted by $\tilde{w} = \tilde{w}(\tilde{x},\tilde{t})$; ρ, A, I, and E_f are, respectively, the density, cross-sectional area, second moment of the area, and the effective Young's modulus. Here, V_p and $\tilde{v}(\tilde{t})$ are, respectively, the applied DC and AC voltages and ε is the

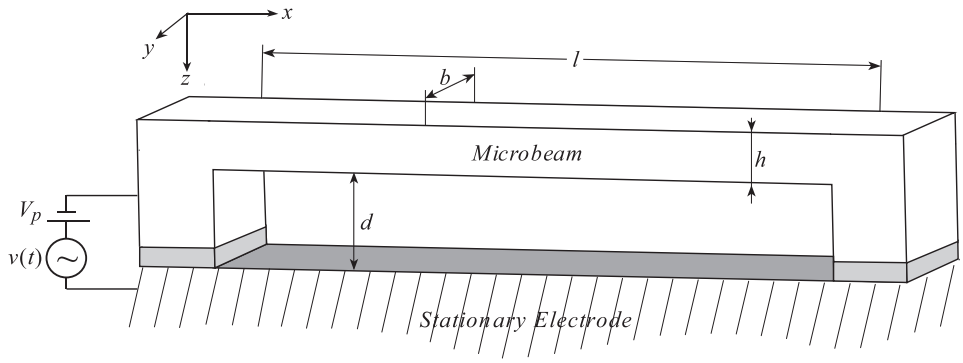

Figure 1. Schematic of the electrostatic microactuator.

Table 1. Microactuator parameters.

l	b	h	d	E_f	$\tilde{N}$	ε
510 μm	100 μm	1.5 μm	1.18 μm	166 GPa	1.56164×10^{-4} N	8.854×10^{-12} F m^{-1}

permittivity. The residual stress due to microfabrication is represented by the axial force $\tilde{N}$. The prime and overdot denote the derivatives with respect to the space coordinate $\tilde{x}$ along the beam length and time $\tilde{t}$, respectively.

For convenience, we define the following nondimensional variables:

$$w = \frac{\tilde{w}}{d}, \quad x = \frac{\tilde{x}}{l}, \quad \text{and} \quad t = \frac{\tilde{t}}{\tau}$$

and the parameters

$$c = \hat{c}\frac{l^2}{\sqrt{E_f I \rho A}}, \quad \alpha_1 = 6\left(\frac{d}{h}\right)^2, \quad \alpha_2 = 6\frac{l^4\varepsilon}{d^3 E_f h^3}, \quad N = \hat{N}\frac{l^2}{E_f I}, \quad \tau = \sqrt{\frac{l^4 \rho A}{E_f I}}.$$

Therefore, equations 1 and 2 can be rewritten in the nondimensional form

$$\ddot{w} + c\dot{w} + w^{iv} = \alpha_2 \frac{[V_p + v(t)]^2}{(1-w)^2} + [\alpha_1 \Gamma(w, w) + N]w'' \tag{3}$$

$$w(0,t) = w(1,t) = 0 \quad \text{and} \quad w'(0,t) = w'(1,t) = 0 \tag{4}$$

Here,

$$\Gamma(f, g) = \int_0^1 f' g' \, dx, \quad v(t) = v_{\text{AC}} \cos(\Omega t),$$

the damping coefficient c is related to the quality factor Q by $Q = \omega/c$, and ω is the natural frequency.

The problem describing the static deflection $w_s(x)$ can be deduced from equations 3 and 4 by dropping the time-dependent terms. The result is

$$w_s^{iv} = \alpha_2 \frac{V_p^2}{(1 - w_s)^2} + [\alpha_1 \Gamma(w_s, w_s) + N]\, w_s'', \tag{5}$$

$$w_s(0) = w_s(1) = 0 \quad \text{and} \quad w_s'(0) = w_s'(1) = 0. \tag{6}$$

The linear undamped eigenvalue problem (EVP) governing the mode shapes and natural frequencies can be obtained by linearizing equations 3 and 4 around the deflected position. It is, therefore, convenient to decompose the total deflection into a static component $w_s(x)$, the solution of equations 5 and 6, and a dynamic component $w_d(x, t)$. Thus, we write

$$w(x, t) = w_s(x) + w_d(x, t). \tag{7}$$

Substituting equation 7 into equation 3, using equations 5, and expanding the result in a third-order Taylor series yields

$$\begin{aligned} w_d^{iv} + \ddot{w}_d + c\dot{w}_d = {} & [\alpha_1 \Gamma(w_s, w_s) + N]\, w_d'' \\ & + \alpha_1 \Gamma(w_d, w_d) \left(w_s'' + w_d''\right) + 2\alpha_1 \Gamma(w_s, w_d) \left(w_s'' + w_d''\right) \\ & + \alpha_2 \left[\frac{2V_p \upsilon(t)}{(1 - w_s)^2} + \frac{\upsilon(t)^2}{(1 - w_s)^2} + \frac{2\left[V_p + \upsilon(t)\right]^2}{(1 - w_s)^3} w_d \right. \\ & \left. + \frac{3\left[V_p + \upsilon(t)\right]^2}{(1 - w_s)^4} w_d^2 + \frac{4\left[V_p + \upsilon(t)\right]^2}{(1 - w_s)^5} w_d^3 \right]. \end{aligned} \tag{8, 9}$$

In case $V_p \gg \upsilon(t)$, equation 9 can be further reduced to

$$\begin{aligned} w_d^{iv} + \ddot{w}_d + c\dot{w}_d = {} & [\alpha_1 \Gamma(w_s, w_s) + N]\, w_d'' + \frac{2\alpha_2 V_p \upsilon(t)}{(1 - w_s)^2} \\ & + \alpha_2 V_p^2 \left[\frac{2w_d}{(1 - w_s)^3} + \frac{3w_d^2}{(1 - w_s)^4} + \frac{4w_d^3}{(1 - w_s)^5} \right] \\ & + \alpha_1 \left(w_s'' + w_d''\right) [\Gamma(w_d, w_d) + 2\Gamma(w_s, w_d)]. \end{aligned} \tag{10}$$

The boundary conditions associated with the dynamic component are

$$w_d(0, t) = w_d(1, t) = 0 \quad \text{and} \quad w_d'(0, t) = w_d'(1, t) = 0. \tag{11}$$

The natural frequencies of the microactuator are solutions of the linear undamped EVP associated with equations 10 and 11. The EVP is formulated by substituting the harmonic form

$w_d(x,t) = \phi(x)e^{i\omega t}$ into equations 10 and 11 and dropping the nonlinear, time-varying, force, and damping terms. The result is

$$\phi^{iv} - \omega^2\phi = [\alpha_1\Gamma(w_s, w_s) + N]\,\phi'' + 2\alpha_1\Gamma(w_s, \phi)w_s'' + 2\alpha_2\phi\frac{V_p^2}{(1-w_s)^3}, \tag{12}$$

$$\phi(0) = \phi(1) = 0 \quad \text{and} \quad \phi'(0) = \phi'(1) = 0, \tag{13}$$

where $\phi(x)$ is the mode shape associated with the frequency ω.

3. DISCRETIZED MODELS

In order to analyze the performance of a microbeam subjected to a combination of DC and AC voltages, we propose to construct a ROM. To this end, the derivative terms in equations 3–6, 12, and 13 are discretized by using the DQM, which uses a discrete-point approximation (Bert and Malik, 1996; Najar et al., 2005) of the deflection rather than the mode-shape decomposition (Nayfeh et al., 2007), which is classically used in the Galerkin method to approximate the response of a flexible structure. We next present the space and time discretizations, DQM and FDM.

3.1. Space Discretization

First, we integrate by parts the integral terms in equations 3–6, 12, and 13, and apply the Newton–Cotes formula and DQM (Najar et al., 2005) to discretize the integral and derivative terms, respectively. We use the notation $w_i(t) = w(x_i, t)$ for the microbeam deflection at the Chebyshev–Gauss–Lobatto discrete grid points

$$x_i = \frac{1}{2}\left[1 - \cos\frac{(i-1)}{(n-1)}\pi\right] \quad (i = 1, 2, \ldots, n).$$

Next, the integral approximation and the DQM are applied to the dynamic, static, and EVP formulations.

3.1.1. ROM Corresponding to Equations 3 and 4

We have

$$\ddot{w}_i + c\dot{w}_i + \sum_{j=1}^{n} A_{ij}^{(4)} w_j = \left[N - \alpha_1 \sum_{j=1}^{n}\sum_{k=1}^{n} C_j w_j A_{jk}^{(2)} w_k\right] \sum_{j=1}^{n} A_{ij}^{(2)} w_j + \alpha_2 \frac{\left[V_p + v(t)\right]^2}{(1-w_i)^2} \quad i = 1, 2, \ldots, n \tag{14}$$

$$w_1 = w_n = 0 \quad \text{and} \quad \sum_{j=1}^{n} A_{1j}^{(1)} w_j = \sum_{j=1}^{n} A_{nj}^{(1)} w_j = 0 \tag{15}$$

where n is the number of DQM grid points. The DQM coefficient matrices $\left[A^{(r)}\right]$ and Newton–Cotes coefficients C_j are given by Najar et al. (2005). The nonlinear ordinary-differential system (equations 14 and 15) can now be used to approximate the microbeam dynamics.

3.1.2. ROM Corresponding to Equations 5 and 6

We have

$$\sum_{j=1}^{n} A_{ij}^{(4)} w_j^s = \alpha_2 \frac{V_p^2}{\left(1 - w_i^s\right)^2} + \left[N - \alpha_1 \sum_{j=1}^{n} \sum_{k=1}^{n} C_j w_j^s A_{jk}^{(2)} w_k^s\right] \sum_{j=1}^{n} A_{ij}^{(2)} w_j^s$$

$$i = 1, 2, \ldots, n, \tag{16}$$

$$w_1^s = w_n^s = 0 \quad \text{and} \quad \sum_{j=1}^{n} A_{1j}^{(1)} w_j^s = \sum_{j=1}^{n} A_{nj}^{(1)} w_j^s = 0, \tag{17}$$

where $w_i^s = w_s(x_i)$ is the static deflection at grid point i. The nonlinear algebraic system of equations 16 and 17 can be used to calculate the static deflection of the microbeam.

3.1.3. ROM Corresponding to Equations 12 and 13

We have

$$-\omega^2 \phi_i + \sum_{j=1}^{n} A_{ij}^{(4)} \phi_j = N \sum_{j=1}^{n} A_{ij}^{(2)} \phi_j - \alpha_1 \sum_{j=1}^{n} A_{ij}^{(2)} \phi_j \left[\sum_{p=1}^{n} \sum_{q=1}^{n} C_p w_p^s A_{pq}^{(2)} w_q^s\right]$$

$$- \alpha_1 \sum_{j=1}^{n} A_{ij}^{(2)} \phi_j \left[\sum_{p=1}^{n} \sum_{q=1}^{n} \sum_{r=1}^{n} C_p A_{pq}^{(1)} A_{pr}^{(1)} w_q^s \phi_r\right]$$

$$+ 2\alpha_2 \phi_i \frac{V_p^2}{\left(1 - w_i^s\right)^3}, \quad i = 1, 2, \ldots, n, \tag{18}$$

$$\phi_1 = \phi_n = 0 \quad \text{and} \quad \sum_{j=1}^{n} A_{1j}^{(1)} \phi_j = \sum_{j=1}^{n} A_{nj}^{(1)} \phi_j = 0, \tag{19}$$

where $\phi_i = \phi(x_i)$. The linear algebraic system of equations 18 and 19 can be solved for the undamped natural frequencies and mode shapes of the microbeam.

3.2. Time Discretization

Equations 14 and 15 are a set of n nonlinear second-order ODEs that describe the microbeam dynamics. The number of equations is first reduced to $(n - 4)$ by substituting for w_1, w_2,

w_{n-1}, and w_n from equations 15 into equations 14. The ROM can then be written as a set of $2(n-4)$ nonlinear first-order ODEs. Taking advantage of the symmetry of the grid-point distribution, the microbeam geometry, and the electrostatic force about the midpoint, we reduce the number of first-order ODEs to $(n-3)$.

To determine periodic responses of the microactuator to AC excitations, we use the FDM (Nayfeh and Balachandran, 1995) to discretize an orbit whose period is $T = 2\pi/\Omega$, where Ω is the excitation frequency. In order to guarantee periodicity, we discretize the orbit using $(m+1)$ points and enforce the condition $w_{i,0} = w_{i,m}$; that is, the first and last points of any orbit (points zero and m) are identical. Consequently, the orbit is time-discretized using m equally spaced points. At each of these points, we have a set of $(n-3)$ ODEs given by

$$\dot{w}_{i,p} = w^{v}_{i,p}$$

$$\dot{w}^{v}_{i,p} = -c w^{v}_{i,p} + \left[N - \alpha_1 \sum_{j=1}^{n} \sum_{l=1}^{n} C_j w_{j,p} A^{(2)}_{jl} w_{l,p} \right] \sum_{j=1}^{n} A^{(2)}_{ij} w_{j,p}$$

$$- \sum_{j=1}^{n} A^{(4)}_{ij} w_{j,p} + \alpha_2 \frac{\left[V_p + v\left(t_p\right) \right]^2}{\left(1 - w_{i,p}\right)^2}$$

$$\text{with } i = 3, 4, \ldots, \frac{(n+1)}{2} \quad \text{and} \quad p = 1, 2, \ldots, m, \tag{20}$$

and $t_p = p\Delta t$ ($\Delta t = T/m$), $w_{i,p} = w(x_i, t_p)$, and $w^{v}_{i,p} = w^{v}(x_i, t_p) = \dot{w}(x_i, t_p)$.

The FDM can now be applied to the system of equation 20 to yield a set of nonlinear algebraic equations. In this case, a two-step explicit central-difference scheme is used to approximate the time derivatives. Therefore, for an n DQM-discretized microbeam and an $(m+1)$ FDM-discretized orbit, the microbeam dynamics can be approximated by a set of $m(n-3)$ nonlinear algebraic equations in $m(n-3)$ unknown displacements and velocities. These equations can be solved for the unknowns using the Newton–Raphson method. The stability of the orbits can then be found using this combined DQM–FDM discretization in conjunction with Floquet theory (Nayfeh and Mook, 1979; Nayfeh and Balachandran, 1995). While the method of characteristic exponents requires the computation of the eigenvalues of an $m(n-3) \times m(n-3)$ matrix, Floquet theory estimates those of an $(n-3) \times (n-3)$ matrix. However, this theory requires the integration of the associated $(n-3)$ vectors to determine the monodromy matrix.

Depending on the type of the limit cycle (primary, superharmonic, or subharmonic) to be determined, we search for periodic orbits corresponding to a forcing frequency Ω; that is, we seek periodic orbits with period T satisfying one of the following conditions (Nayfeh and Mook, 1979; Nayfeh and Balachandran, 1995):

- $T = 2\pi/\Omega$ for a primary or all superharmonic resonances;
- $T = 2\pi k/\Omega$ for a subharmonic resonance of order k.

Table 2. Loading cases.

	V_p	Stable $w_s(1/2)$	Unstable $w_s(1/2)$	ω_1	v_{AC}	Q
Case 1	2.0 V	0.0353	0.8849	23.95	0.05 V	300
Case 2	2.0 V	0.0353	0.8849	23.95	0.5 V	1000
Case 3	3.5 V	0.1253	0.7511	21.98	0.1 V	300
Case 4	3.5 V	0.1253	0.7511	21.98	1.0 V	1000

4. LIMIT-CYCLE SOLUTIONS OF THE FIRST MODE

In order to analyze hardening and softening behaviors, of the microactuator at hand subject to small and large excitations, we simulate the microbeam response using the four loading cases given in Table 2. The sign of the effective nonlinearity coefficient, indicating a transition from hardening-type to softening-type as the applied DC voltage increases, changes at $V_p = 3.27$ V (Abdel-Rahman et al., 2005). The microbeam experiences static pull-in at 4.75 V (Najar et al., 2005).

The static deflection $w_s(x)$ is obtained by solving equations 16 and 17 using nine grid points. Owing to the model nonlinearities, stable and unstable solutions are obtained. The natural frequencies are computed by solving the linear undamped EVP when the stable $w_s(x)$ is substituted into equation 18.

Previous works (Najar et al., 2005, 2006) have proved that using nine grid points accurately estimates the linear natural frequencies and small oscillations. For large oscillations, the use of nine points results in a small error (approximately 4%). Therefore, using at least nine grid points (three coupled second-order ODEs) and 100 time steps leads to acceptable convergence of the lower and upper branches of the frequency-response curve and a globally valid approximation of the microbeam motions. For simulation purposes, the numbers of grid points and time steps are fixed to 9 and 100, respectively.

4.1. Primary Resonance

4.1.1. Local Hardening-type Behavior

For a period $T = 2\pi/\Omega$, Figure 2 shows the maximum deflection at the beam midpoint (W_{max}) for limit cycles obtained for loading Case 1 as the excitation frequency of the AC voltage is varied near the fundamental natural frequency $\Omega \approx \omega_1$. We apply Floquet theory to ascertain the stability of these limit cycles. These results are in full agreement with those reported by Nayfeh et al. (2007) for the same microbeam. In fact, the frequency-response curve shows a hardening-type behavior for small orbits. For large orbits, the behavior is dominated by the electrostatic force and, thus, the system exhibits a softening-type behavior. Therefore, the system behavior is locally of the hardening type and globally of the softening type. We note that the frequency-response curve is composed of five branches A, B, C, D, and E. The solution is stable on branches A, C, and E and unstable on branches B and D. In addition, there are three cyclic-fold bifurcation points at $\Omega = 24.17$, 24.58, and 24.67 that separate branches C and D, A and B, and D and E, respectively, where one of the Floquet multipliers exits the unit circle through $+1$. Resonators operating within the

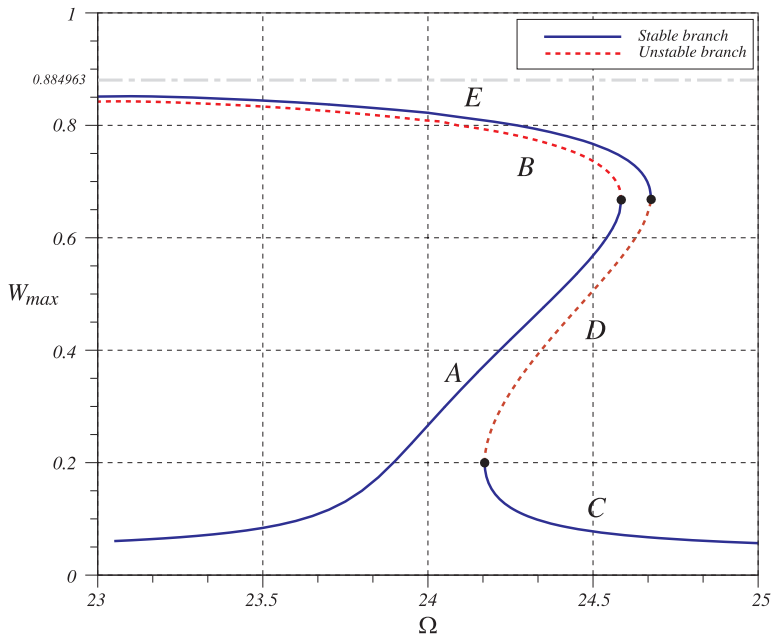

Figure 2. Local hardening-type behavior of the microactuator for loading Case 1.

frequency interval (24.17, 24.67) are susceptible to jumps, hysteretic behavior, and dynamic pull-in, all of which are undesirable for MEMS actuators. In Figure 2, the gray dashed-dotted line denotes the limit of stability defined by the unstable static deflection (saddle).

To uncover some of the interesting dynamic phenomena in the microactuator response, we use large values of the excitation amplitude and quality factor and solve equation 20 for a period $T = 2\pi/\Omega$ and loading Case 2. We compute limit cycles and generate the frequency-response curve shown in Figure 3. A comparison of Figures 2 and 3 indicates that increasing the forcing amplitude and quality factor augments the pull-in band, which is the frequency band in the frequency-response curve where no stable solutions exist (Najar et al., 2006) and, hence, dynamic pull-in is more likely to occur. This is in agreement with the conclusion by Nayfeh et al. (2007) that increasing the AC voltage increases the pull-in band. Because the total applied voltage for loading Case 2 is larger than that in Case 1, the effective nonlinearity decreases and the zone of hardening-type behavior is reduced. As a result, the region of stable motions in the neighborhood of the fundamental natural frequency is smaller than that in Case 1, especially for branch E. In addition, spikes are found within similar ranges of frequency on branches B and E of Figure 3. The solutions along these spikes are unstable because of dynamic pull-in on branch B and the maximum deflections of these orbits exceed the unstable static deflection (saddle) on branch E. Spikes, described as singularities, were first identified by Nayfeh and Younis (2005) in the case of a subharmonic resonance of order one-half of the first mode with a softening-type behavior. However, they did not characterize them or discuss their origin.

To characterize these spikes, we display in Figures 4 and 5 the dynamic responses of the system for points on these spikes. At each point, the phase portraits, time histories, and

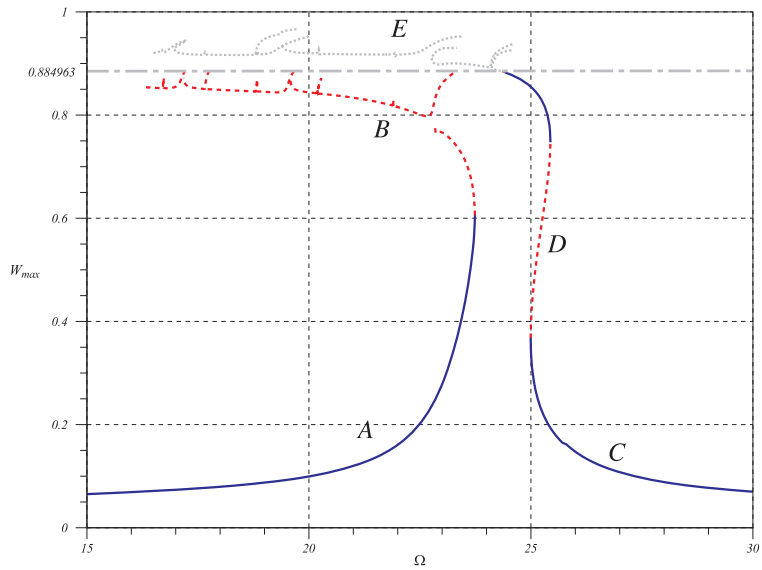

Figure 3. Frequency-response curve of the microbeam for loading Case 2.

power spectra show *simultaneous resonances* of the first mode and a higher mode (Nayfeh and Mook, 1979). We note that $W_{\max}$ is the maximum value of the midpoint deflection w_5 for a particular orbit, Δw is the size of the orbit defined as the absolute difference between the rightmost and leftmost points of the orbit in the phase portrait, and p is the variable representing the discrete nondimensional time from equation 20.

The peaks in the power spectra suggest that superharmonics of the third mode of order eight (Figure 4a), order seven (Figure 4b), and order six (Figure 4c) are present in the spikes along branch E. In fact, the mode associated with these resonances is identified by multiplying the excitation frequency by the order of the superharmonic as follows: $17.11 \times 8 = 136.88$, $19.40 \times 7 = 135.8$, and $22.77 \times 6 = 136.62$, respectively. On the other hand, solving the linear eigenvalue problem described by equations 18 and 19 for loading Case 2 with nine grid points, we obtain $\omega_1 = 23.95$, $\omega_2 = 65.16$, $\omega_3 = 132.59$, and $\omega_4 = 195.20$. Therefore, we conclude that the solutions along the spikes, in branches B and E, correspond to simultaneous resonance of the first and third modes.

Similarly, spikes corresponding to simultaneous resonances of the first and fourth modes occur on branches B and E of Figure 3. Orbits, on branch E, corresponding to some points on these spikes are shown in Figure 5. The orders of the superharmonic resonance of the fourth mode are identified from the power spectra as 12, 11, 10, and 9 for Figures 5a–d, respectively. The frequency of the mode interacting with the primary resonance of the first mode in these figures is found in the range between 217.35 and 225.96, nearly corresponding to the natural frequency of the fourth mode. The difference between this frequency range and the value $\omega_4 = 195.20$ obtained above is due to the use of only 100 points in the FDM discretization, which are not sufficient to accurately resolve the higher modes.

Orbits that exit their safe basins, resulting in dynamic pull-in due to large perturbations, are globally unstable. On the other hand, the local stability of limit-cycle solutions can be

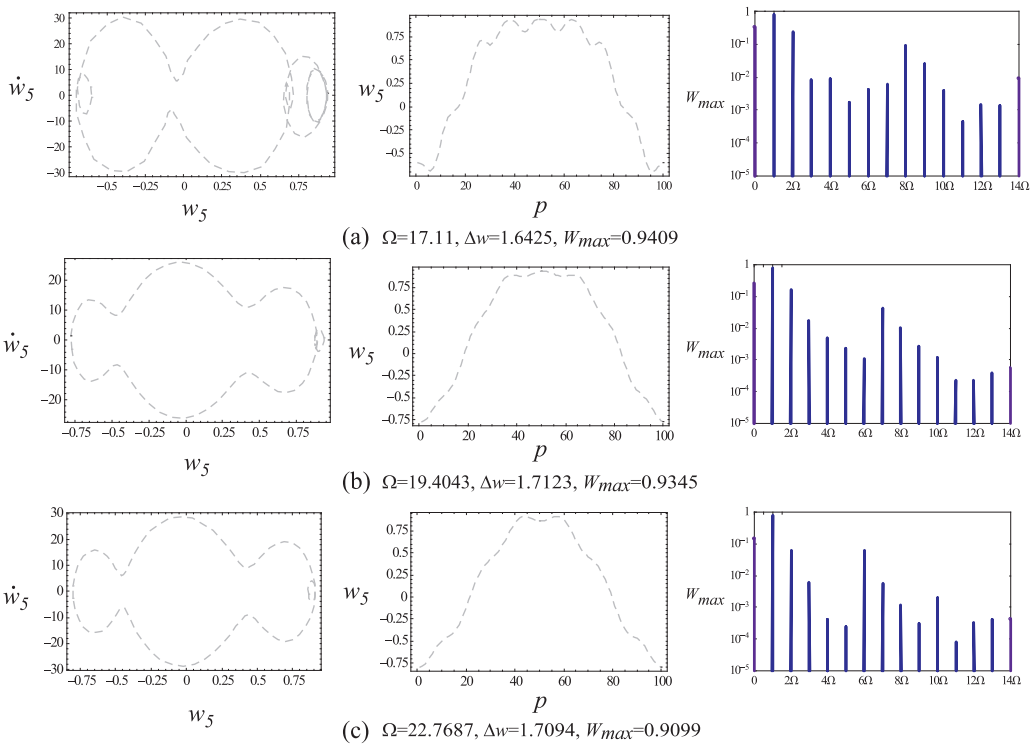

Figure 4. Phase portraits, time-histories, and power spectra of the simultaneous resonances found along branch E of Figure 3: primary resonance of the first mode and superharmonic resonances of the third mode of (a) order 8, (b) order 7, and (c) order 6.

examined using Floquet theory. For globally unstable limit cycles, such as the points above the saddle in Figure 3, the gray dashed-dotted line at $W_{\max} = 0.886943$, and henceforth, the Floquet multipliers corresponding to these limit cycles are six complex eigenvalues inside the unit circle, indicating incorrectly that the orbits are stable. This means that the calculated orbits are not accurate enough, as evident from their nonsmoothness. In fact, in this case, very large amplitudes of motion ($W_{\max} > 0.88$) are observed, which degrade the quality of the approximate solutions. An example of the inaccuracy introduced by the FDM is shown in Figure 7. A large orbit taken from Figure 6 is computed using 100, 200, and 300 points in the FDM discretization. The results show that the maximum deflection converges as m is increased. In addition, the Floquet multipliers tend to exit the unit circle through $+1$ as the orbit is more accurately approximated, which is in agreement with long-time integration results.

To overcome the inaccuracy of the FDM solution in determining the local stability, we use long-time integration. We find the periodic orbits first using the DQM–FDM technique, then inject the states of one point on the orbit into a long-time integration of the ODE system in equations 14 and 15 and examine whether the numerical solution settles down on the orbit or not. Using *Mathematica*, we carried out numerical integration to simulate the microactuator response at a frequency beyond the crossing point *CP*, shown in Figure 6, leading to an

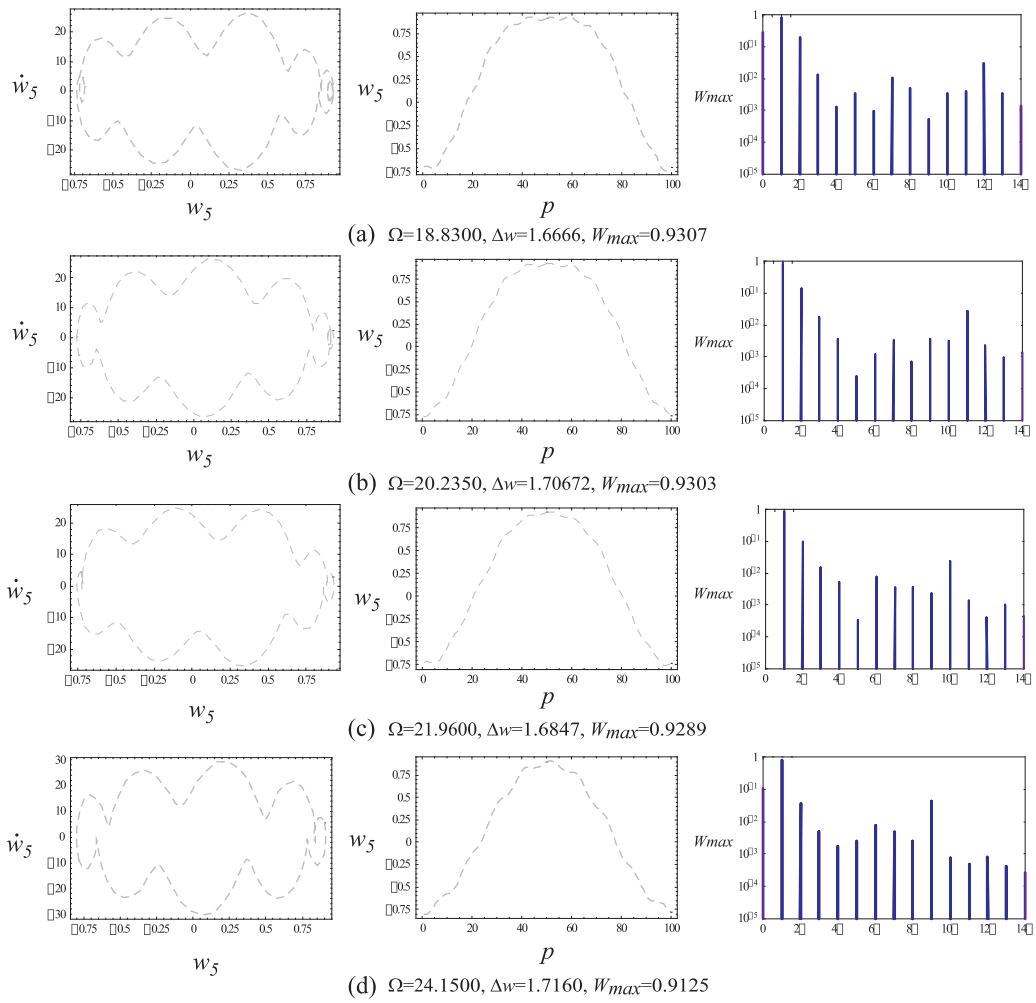

Figure 5. Phase portraits, time histories, and power spectra of the simultaneous resonances found along branch E of Figure 3: primary resonance of the first mode and superharmonic resonances of the fourth mode of (a) order 12, (b) order 11, (c) order 10, and (d) order 9.

unstable response. Figure 6 also shows that the instability exists from CP at $\Omega = 24.3$ to 24.42. In order to explain this, the microactuator responses at $\Omega = 24.42$ and 24.43 are displayed in Figures 8 and 9, respectively. We used long-time integration to determine the local stability of the orbits. The results at $\Omega = 24.43$, shown in Figure 9, particularly the phase portrait in Figure 9d and time history in Figure 9e, indicate that the solution is bounded and stable. This is confirmed by convergence of the solution towards a one-period limit cycle, as shown by the Poincaré section in Figure 9f.

On the other hand, long-time integration shows that the solution at $\Omega = 24.42$, Figure 8, is unstable. Two stages are observed in the phase portrait, Figure 8d. First, before the instability occurs, the orbit wanders in the phase plane. Second, dynamic pull-in occurs when

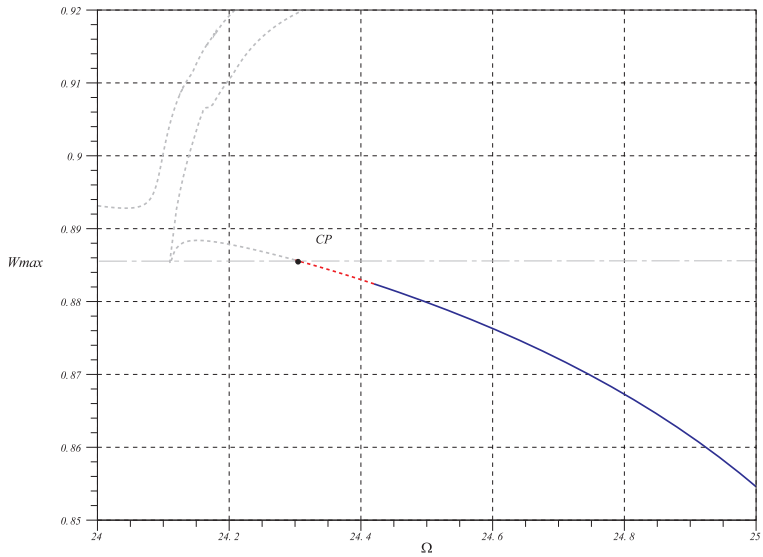

Figure 6. Zoom near the crossing point at $\Omega = 24.3$ in Figure 3.

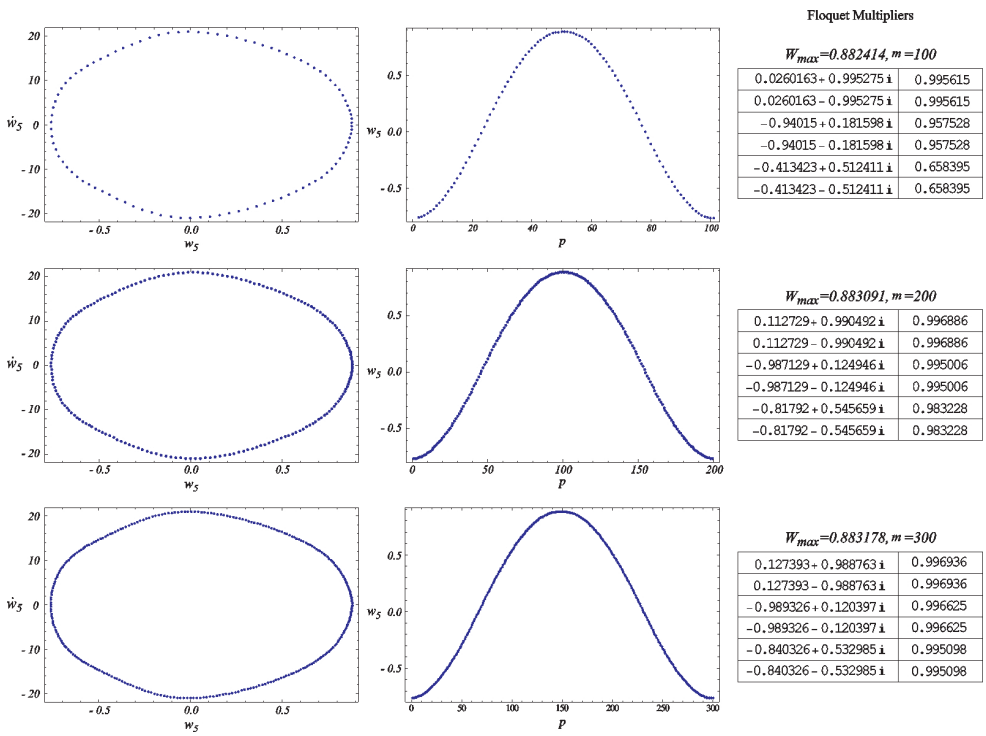

Figure 7. Comparison among three DQM–FDM solutions obtained at $\Omega = 24.42$ for $m = 100$, 200, and 300 in Figure 3.

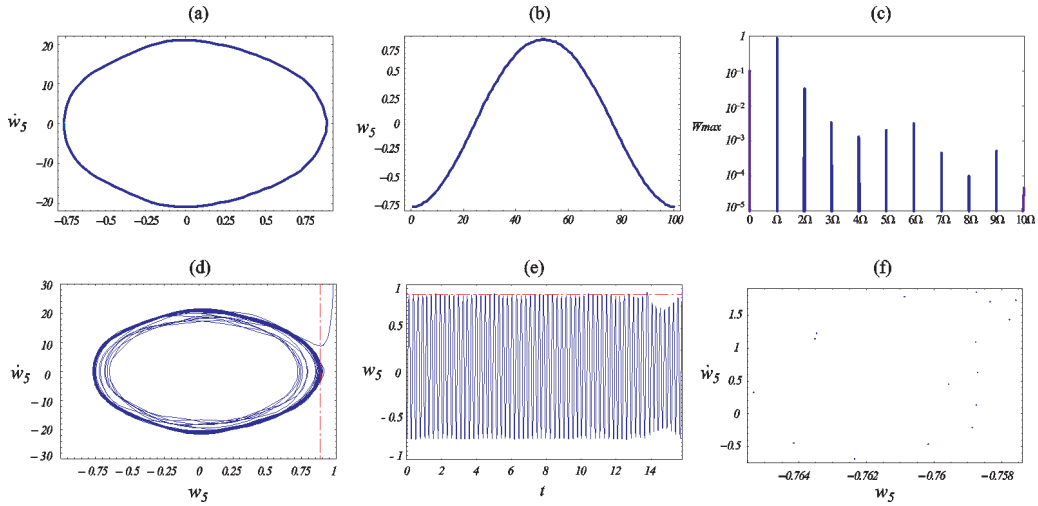

Figure 8. Comparison between the DQM–FDM and long-time integration solutions at $\Omega = 24.42$: (a) phase portrait, (b) time history ($W_{\max} = 0.882414$), and (c) power spectra for the DQM–FDM; (d) phase portrait, (e) time history ($W_{\max} > 0.882414$), and (f) Poincaré map for long-time integration.

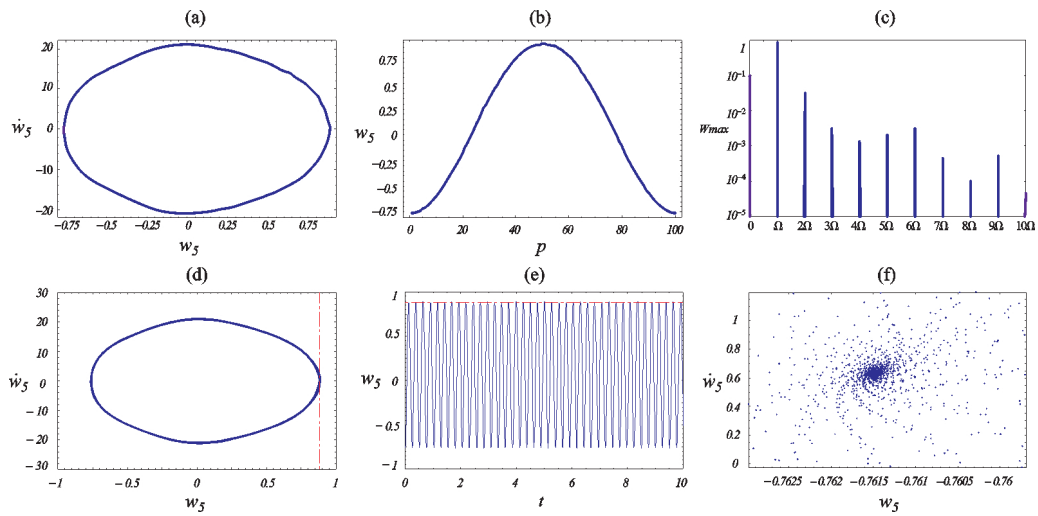

Figure 9. Comparison between the DQM–FDM and long-time integration solutions at $\Omega = 24.43$: (a) phase portrait, (b) time history ($W_{\max} = 0.882114$), and (c) power spectra for the DQM–FDM; (d) phase portrait, (e) time history, and (f) Poincaré map for long-time integration.

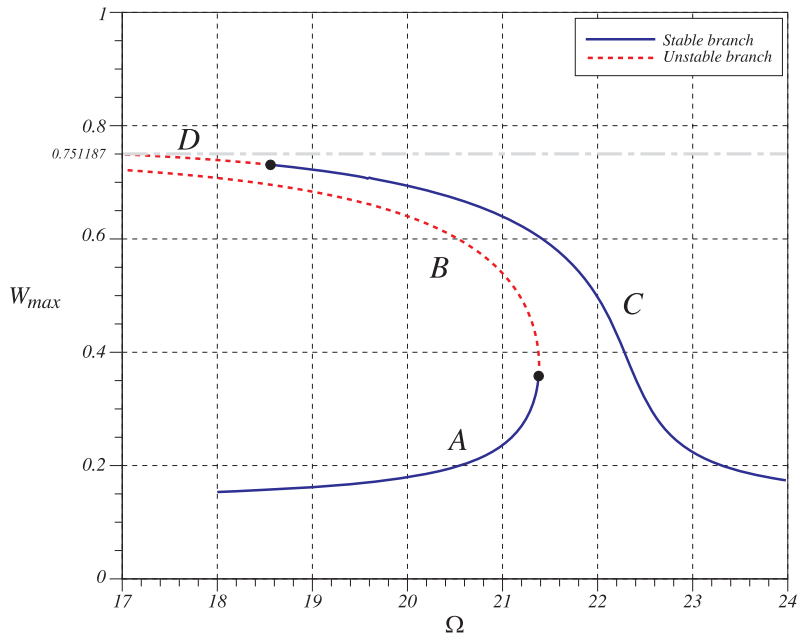

Figure 10. Frequency-response curve of the microbeam for loading Case 3.

the orbit touches the stable manifold of the saddle. As a result, the manifold takes the orbit towards the saddle. When the orbit approaches the saddle, the saddle repels it away along the unstable manifold towards pull-in, thereby producing the "neck" evident directly above the saddle location in the phase portrait, Figure 8d. We note that the orbit crosses the marginal stability line (the dashed-dotted line representing the saddle) during the first phase without the occurrence of pull-in. This crossing might be the result of either a shift in the location of the saddle due to the AC loading and/or of the projection of the six-dimensional phase portrait onto a two-dimensional plane.

4.1.2. Softening-type Behavior

For loading Case 3, Figure 10 displays the frequency-response curve of the microbeam. In this case, the system behavior is locally and globally of the softening type. The frequency-response curve is characterized by four branches of solutions: stable branches A and C and unstable branches B and D. It can be observed that there is only one cyclic-fold bifurcation point, instead of three, and consequently the pull-in band has disappeared. Moreover, there is a period-doubling bifurcation point separating branches C and D with one of the Floquet multipliers leaving the unit circle through -1. The resulting two-period ($2T$) solution is initially stable but quickly loses stability as the frequency is reduced, resulting in dynamic pull-in. The gray dashed-dotted line in Figure 10 denotes the limit of stability defined by the unstable static deflection (saddle). These results are in agreement with those reported by Nayfeh et al. (2007).

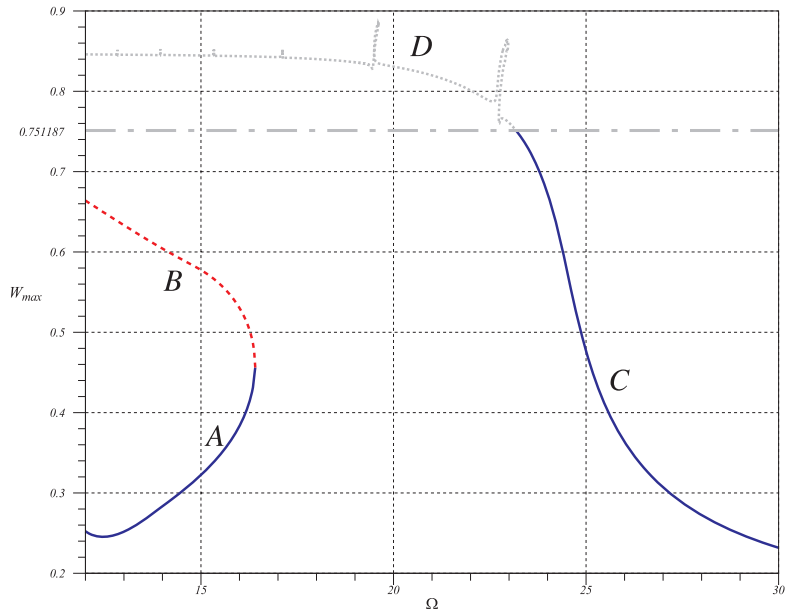

Figure 11. Frequency-response curve of the microbeam for loading Case 4.

We now consider loading Case 4 to obtain a frequency-response curve with locally and globally softening-type behavior. Increasing both the AC voltage and quality factor (Figure 11) widens the instability zone where the only available solution is dynamic pull-in. Spikes similar to those found in the hardening-type case occur.

The simultaneous resonances underlying the spikes are further examined in Figure 12. As the excitation frequency approaches one of the superharmonics of a higher mode, new branches emerge along the unstable branch D, representing simultaneous resonances where primary resonance of the first mode and superharmonic resonance of a higher mode coexist. Solving the linear eigenvalue problem associated with loading Case 4 using nine grid points yields the first four nondimensional natural frequencies 21.97, 64.57, 132.37, and 195.13. The resonances at 22.9 and 19.545, when multiplied by their respective orders six and seven, yield 137.4 and 136.815, indicating superharmonic resonances of orders six and seven of the third mode.

The stable orbits are bounded by the saddle $W_{\max} < 0.751187$ for loading Case 4 (Table 1). Similarly to the locally hardening-type behavior, the Floquet multipliers do not detect the instability of the orbits that exceed the saddle, and thus long-time integration is used for further investigation. In Figures 13 and 14, we compute the orbits using the DQM–FDM technique and determine their stability using long-time integration at a point to the left of the crossing point shown in Figure 11 ($\Omega = 23.005$) and a point to its right ($\Omega = 23.01$), respectively. The solutions are found to be unstable at $\Omega = 23.005$ and stable at $\Omega = 23.01$. Figure 13 depicts the inaccuracy of the saddle obtained using the static equation, since the calculated orbit (Figure 13d) is largely crossing the marginal stability line (the dashed-dotted line representing the saddle) without going to pull-in.

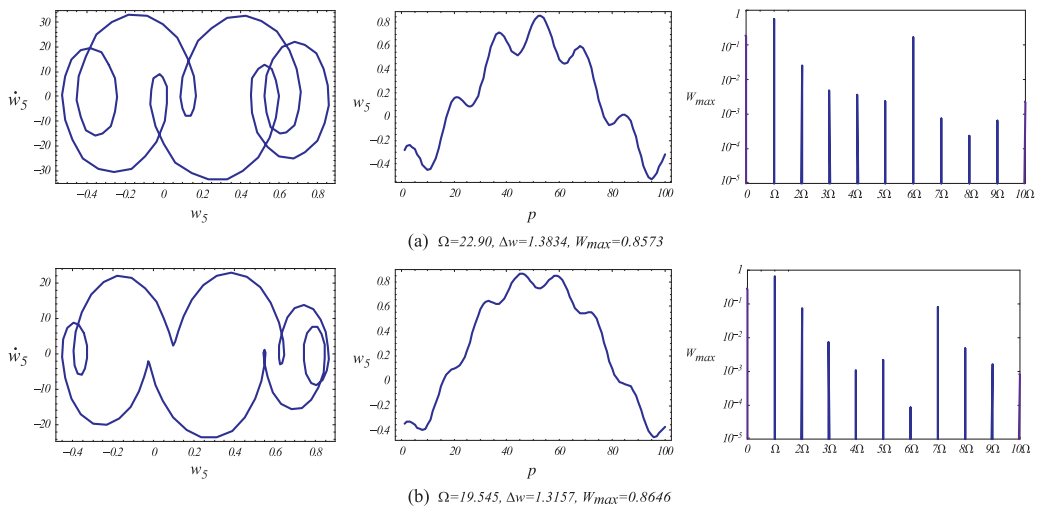

Figure 12. Phase portraits, time histories, and power spectra of the simultaneous resonances near those observed in Figure 3. Superharmonic resonances of the third more of (a) order six and (b) order seven.

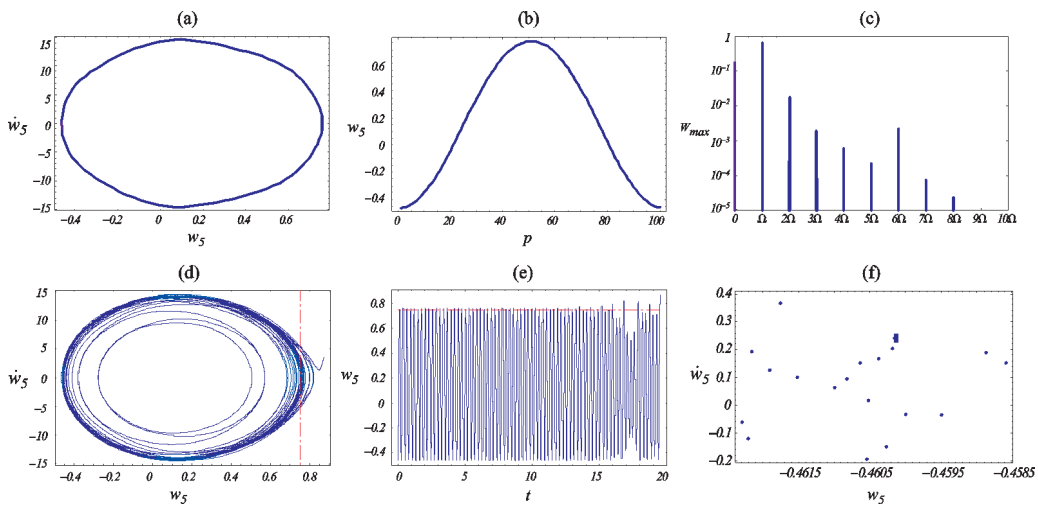

Figure 13. Comparison between the DQM–FDM and long-time integration solutions at $\Omega = 23.005$: (a) phase portrait, (b) time history ($W_{\max} = 0.760634$), and (c) power spectra for the DQM–FDM; (d) phase portrait, (e) time history ($W_{\max} > 0.760634$), and (f) Poincaré map for long-time integration.

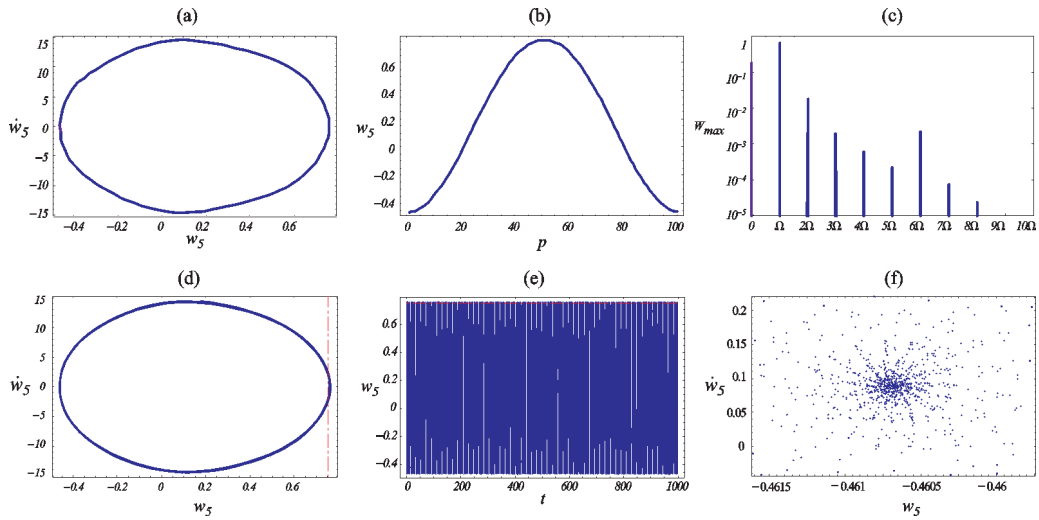

Figure 14. Comparison between the DQM–FDM and long-time integration solutions at $\Omega = 23.01$: (a) phase portrait, (b) time history ($W_{\max} = 0.760402$), and (c) power spectra for the DQM–FDM; (d) phase portrait, (e) time history, and (f) Poincaré map for long-time integration.

4.2. Secondary Resonances of the First Mode

4.2.1. Superharmonic Resonances

Using the period $T = 2\pi/\Omega$, all available superharmonic resonances are identified as the excitation frequency is swept over a wide range of values below ω_1. Loading Cases 2 and 4 are considered to illustrate local hardening-type and softening-type behaviors, respectively.

Local Hardening-type Behavior The frequency-response curve for loading Case 2 (Figure 15) shows a locally hardening-type behavior. We note the appearance of three superharmonic resonances of order two, three, and four at approximately $\frac{1}{2}\omega_1$, $\frac{1}{3}\omega_1$, and $\frac{1}{4}\omega_1$ in the frequency spectrum, respectively. The superharmonic resonances are multi-frequency responses that appear in the neighborhood of ω_1/k for $k = 2, 3$, and 4. These responses are composed of a resonant component at ω_1 and a forced component at $\Omega \approx \omega_1/k$. Dynamic pull-in and a narrow pull-in band are observed in the neighborhood of the superharmonic resonance of order two only. Phase portraits, time histories, and power spectra of the response in the neighborhood of each of the three superharmonic resonances are shown in Figure 16. We note that the phase portrait of the superharmonic resonance of order-k displays k loops because of the k-multiplicity between the periods of the resonant and forced components.

Simultaneous resonances, similar to those obtained in the neighborhood of the first natural frequency, appear on the upper branches of the frequency-response curve of the superharmonic resonance of order two shown in Figure 17. We study these simultaneous resonances by presenting the phase portraits, time histories, and power spectra at selected points on these spikes in Figure 18. Multiplying each frequency by its respective order yields values near 75, which corresponds to the superharmonic of order two of the third mode. There-

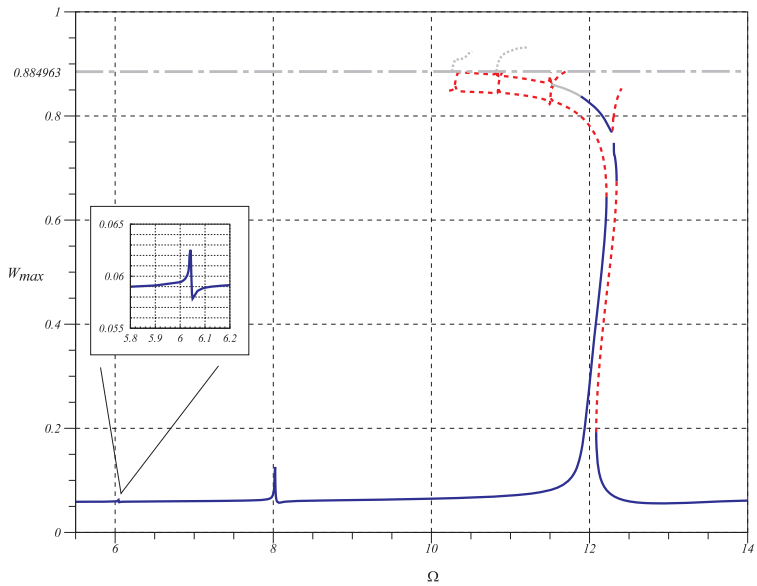

Figure 15. Frequency-response curve for superharmonic resonance of the microbeam for loading Case 2.

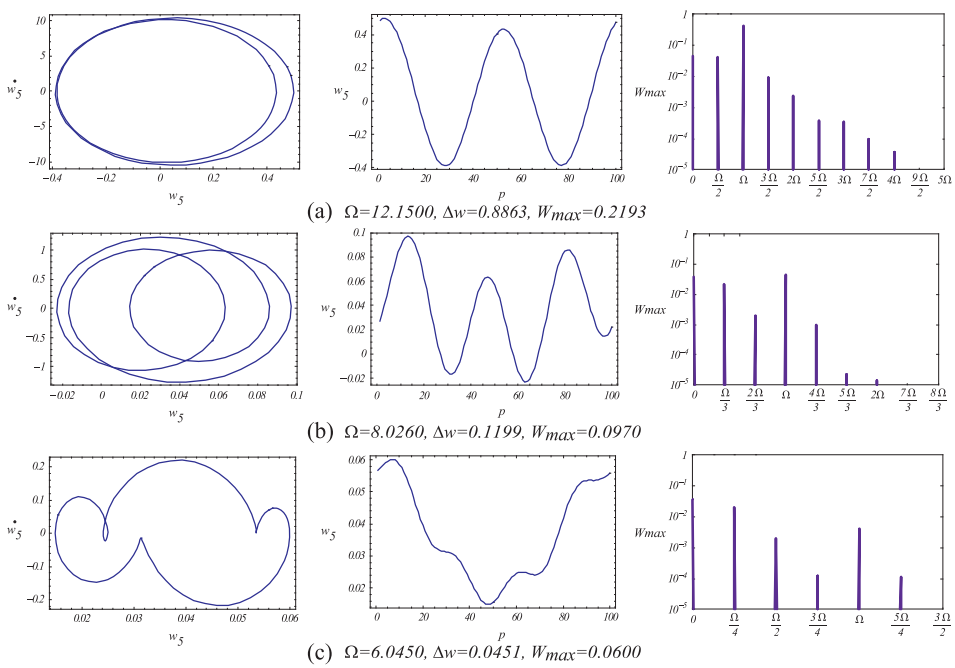

Figure 16. Phase portraits, time histories, and power spectra of the superharmonic resonances of (a) order two, (b) order three, and (c) order four for loading Case 2.

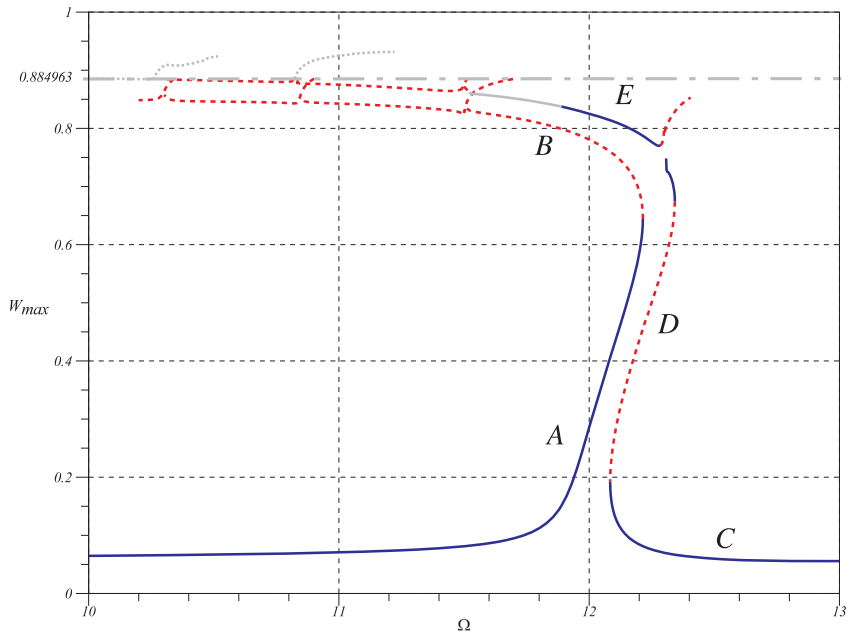

Figure 17. Frequency-response curve of superharmonic resonance of order two for loading Case 2.

fore, the simultaneous resonances are activated by the superharmonics of the first and third modes.

Similar to the case of primary resonance, the stability results obtained from the Floquet multipliers and long-time integration are found to be in disagreement for large orbits. The gray lines in Figure 15 represent solutions predicted by Floquet theory to be stable, but confirmed using the long-time integration to be unstable. The transition point between stable and unstable large orbit solutions, in Figures 15 and 17, occurs at $\Omega = 11.88$. Figures 19 and 20 display the phase portrait, time history, and power spectra obtained using the DQM–FDM only and the phase portrait, time history, and Poincaré map obtained using a combination of the DQM–FDM and long-time integration for a point to the right of ($\Omega = 11.89$) and a point to the left ($\Omega = 11.875$) of the transition point, respectively. The phase portraits, Figures 19d and 20d, show that the limit-cycle solutions are stable and unstable, respectively, and that dynamic pull-in occurs in the second case when the dynamic orbit touches the stable manifold of the saddle.

Softening-type Behavior We use loading Case 4 to analyze superharmonic resonances for a microactuator with a softening-type behavior. Figure 21 shows the frequency-response curve, including large orbits, for frequencies lower than the fundamental natural frequency. The location of the saddle is shown by the gray dashed-dotted line in Figure 21. Ten superharmonic resonances of the first mode are distinguished ranging from order 2 to order 11. The appearance of higher-order superharmonic resonances in loading Case 4 not observed in loading Case 3 is due to the larger DC and AC voltages used in this case. The first six superharmonic resonances, of order two to order seven, exhibit dynamic pull-in and

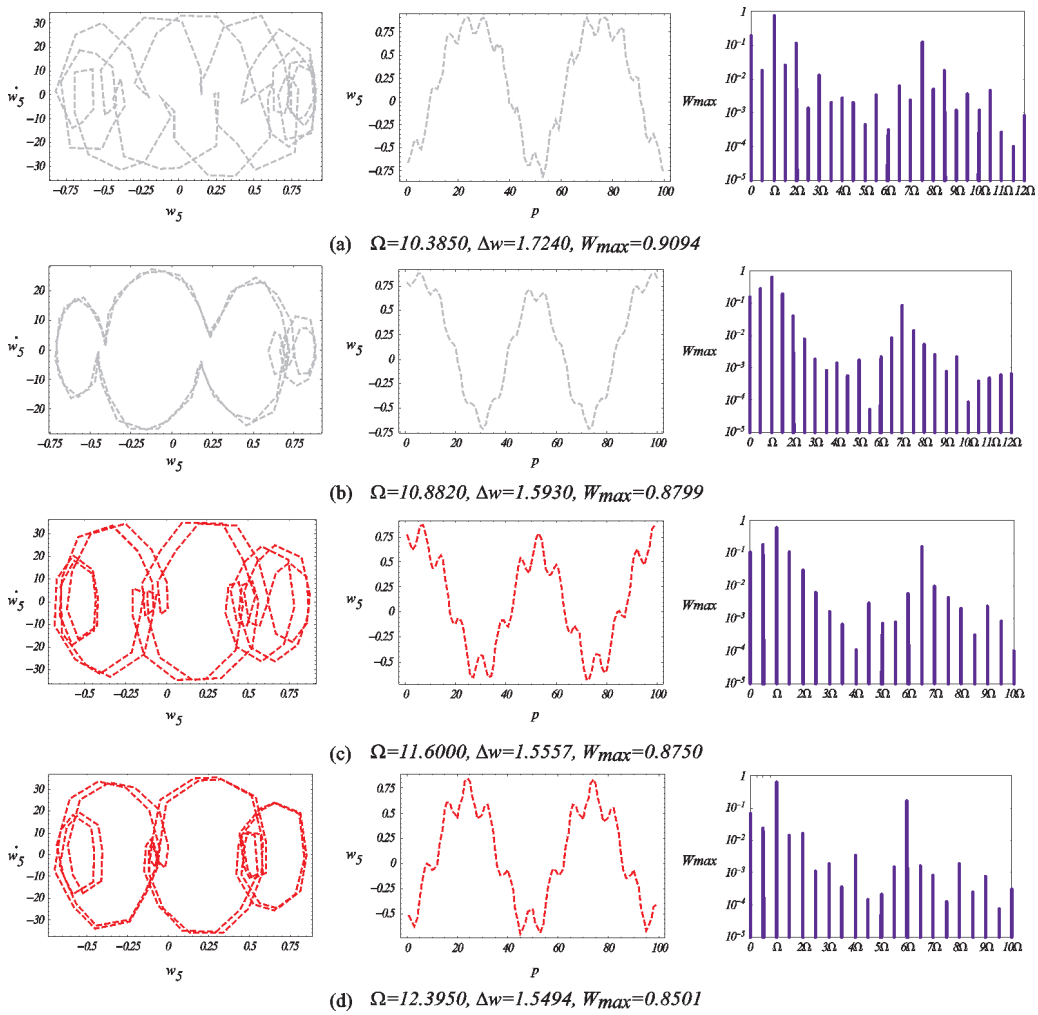

Figure 18. Phase portraits, time histories, and power spectra of the simultaneous resonances in the neighborhood of the superharmonic resonance of order two.

the frequency-response curve has a similar structure in their neighborhood as depicted by Figure 21. We note that the width of the resonance zone for these superharmonics decreases with the order of the resonance. The order of the superharmonic resonances in Figure 21 can be extracted from Figure 22.

4.2.2. Subharmonic Resonance

We now examine the system performance near subharmonic resonances by finding the limit cycles for excitation frequencies larger than ω_1. In this case we let $T = 2k\pi/\Omega$, where $1/k$ denotes the order of the subharmonic to be simulated.

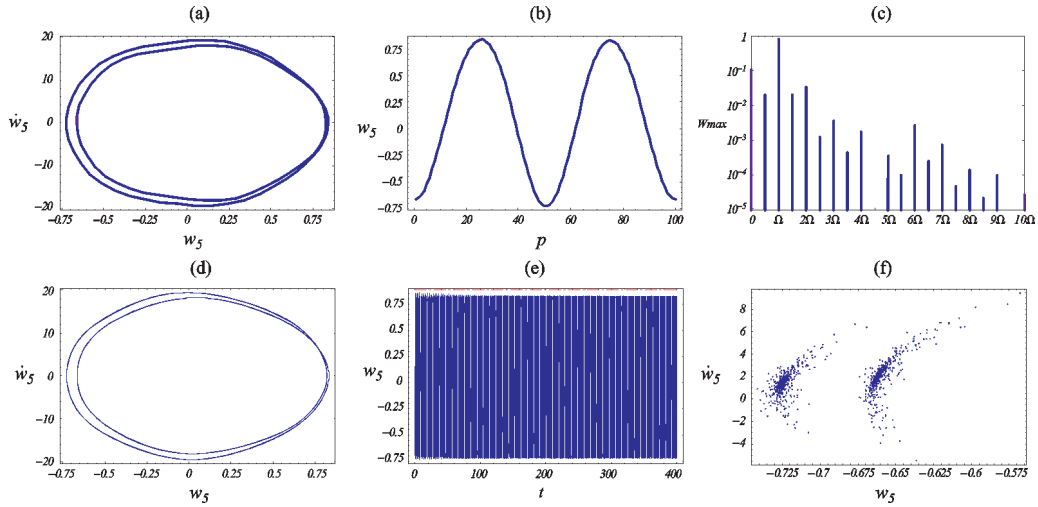

Figure 19. Comparison between the DQM–FDM and the long-time integration solutions at $\Omega = 11.89$: (a) phase portrait, (b) time history ($W_{\max} = 0.837393$), and (c) power spectra for the DQM–FDM; (d) phase portrait, (e) time history, and (f) Poincaré map for long-time integration.

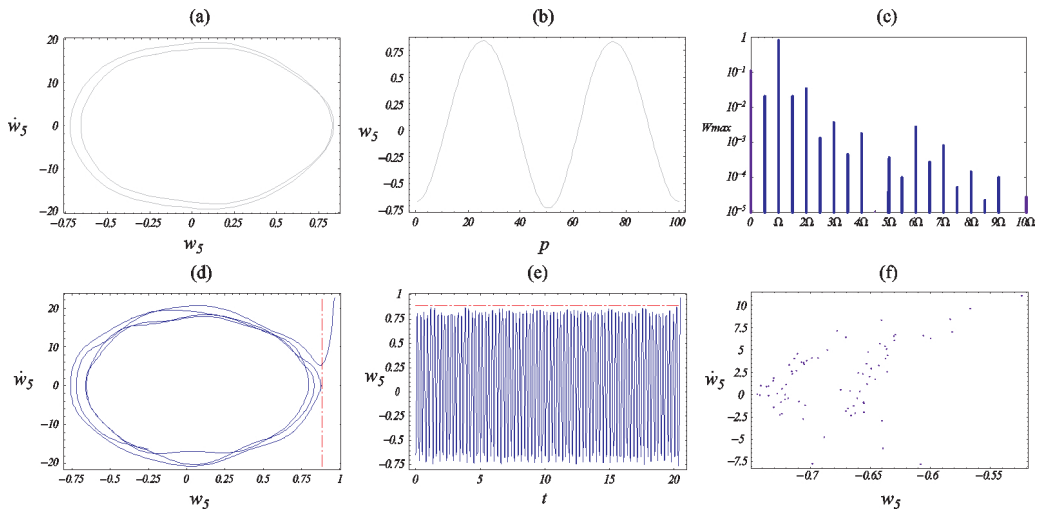

Figure 20. Comparison between the DQM–FDM and the long-time integration solutions at $\Omega = 11.875$: (a) phase portrait, (b) time history ($W_{\max} = 0.838787$), and (c) power spectra for the DQM–FDM; (d) phase portrait, (e) time history ($W_{\max} > 0.838787$), and (f) Poincaré map for long-time integration.

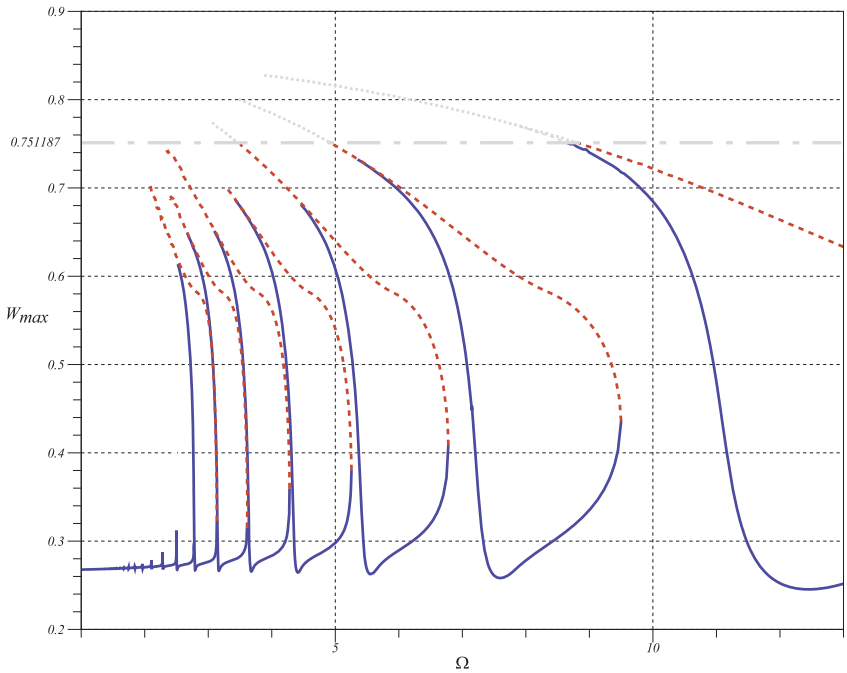

Figure 21. The frequency-response curve of the superharmonic resonances of the microactuator for loading Case 4.

Local Hardening-type Behavior Loading Case 2 yields the frequency-response curve shown in Figure 23, which is typically for a local hardening-type behavior. It exhibits a subharmonic resonance of the first mode of order one-half. The curve is qualitatively similar to that obtained in Figure 3 with five main branches separated by three bifurcation points. Dynamic pull-in is also observed in Figure 23 and a pull-in band is present in the frequency-response curve. Spikes are also observed along branches B and E, depicting simultaneous resonances of the subharmonics of the first and higher modes.

Softening-type Behavior Figure 24 shows the subharmonic resonance of order one-half of the first mode for loading Case 4. The frequency-response curve has a similar structure to that of primary resonance under softening-type behavior. For the same loading case, Figure 25 displays the subharmonic of order one-third of the first mode. As in the case of subharmonic resonance of order one-half, we obtain a softening-type behavior with dynamic pull-in and simultaneous resonances along the upper branches. The subharmonic resonances under softening-type behavior depict larger stretches of the frequency spectrum where the only available solution is pull-in compared with local hardening-type behavior. This behavior is suitable for microswitch applications in which case any excitation frequency within this zone can be used as an actuation signal. In the case of primary resonance, Figure 11 depicts a zone of width 6.77. The corresponding widths associated with the subharmonics of orders one-half and one-third are found to be 13.56 in Figure 24 and 20.35 in Figure 25.

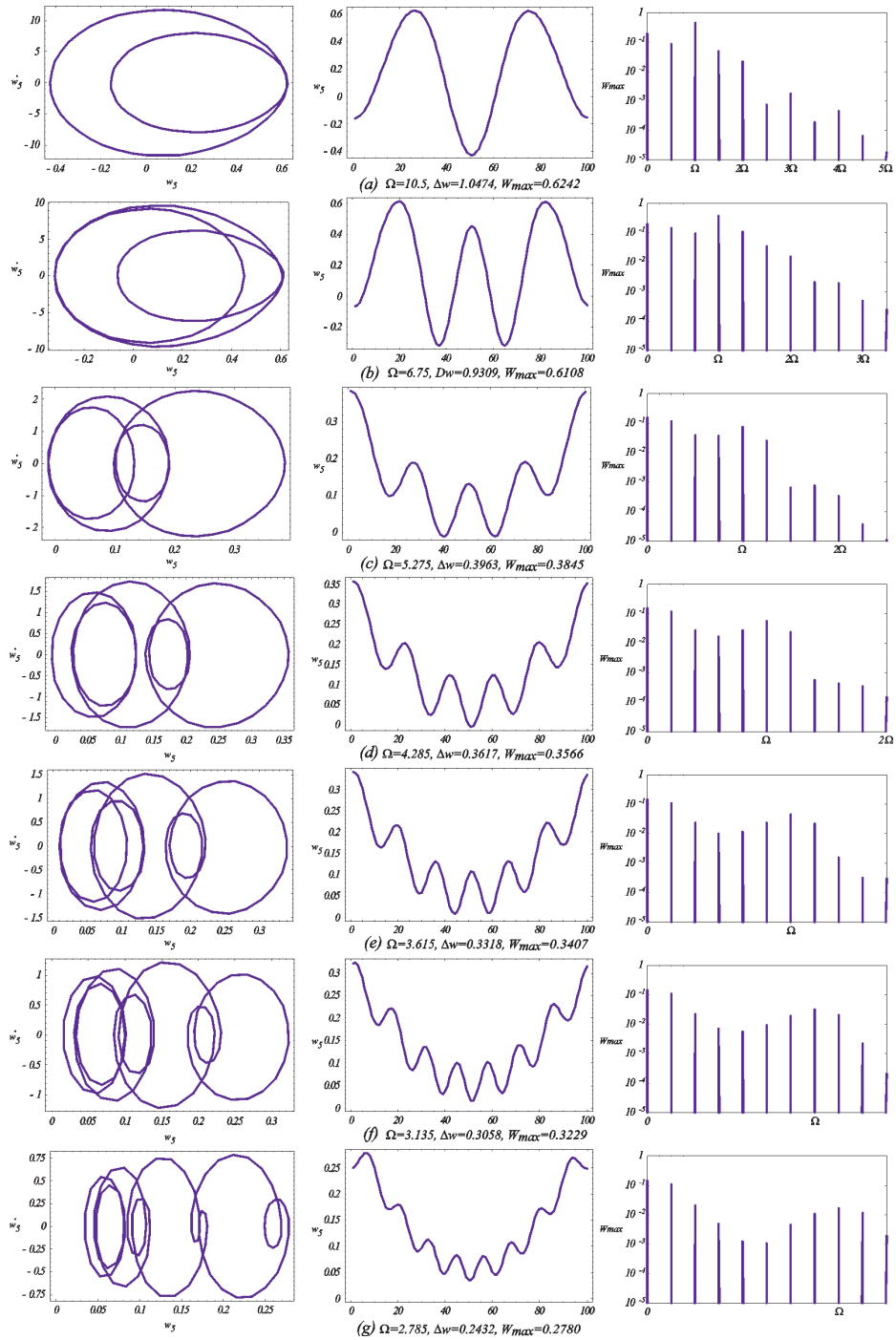

Figure 22. Phase portraits and time-histories of the superharmonic resonances of (a) order two, (b) order three, (c) order four, (d) order five, (e) order six, (f) order seven, and (g) order eight for loading Case 4.

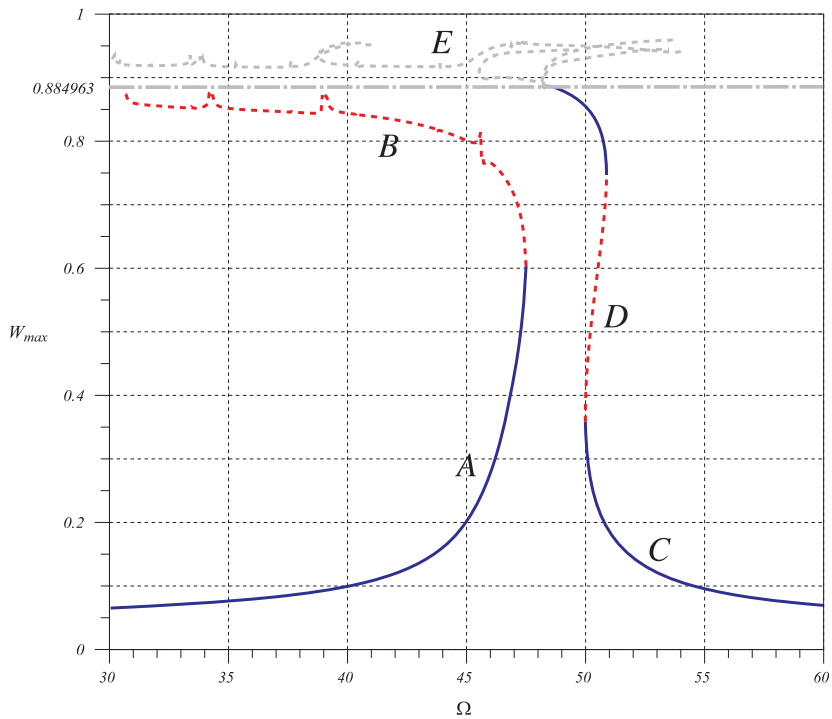

Figure 23. Frequency-response curve for the subharmonic resonance of order $\frac{1}{2}$ of the microactuator under loading Case 3.

5. CONCLUSIONS

We have used a technique that combines DQM and FDM to discretize dynamical continuous systems and have used it to compute limit-cycle solutions of electrostatic microactuators. The technique transforms a partial–differential–integral equation of motion and associated boundary conditions into a set of nonlinear algebraic equations. The solution of these equations yields the vector of state variables along a periodic orbit. The proposed technique was validated by comparing its results with those of models reported previously. We have also confirmed that it is numerically stable and does not suffer from problems related to stiffness and sensitivity to initial conditions.

The combined DQM–FDM technique was used to generate frequency-response curves of a microactuator for large excitations and over a wide frequency range for resonators with either locally hardening or softening behavior. In the first case, the frequency-response curves are bent to the right (i.e. hardening behavior) for small orbits and bent to the left (i.e. softening behavior) for large orbits. Consequently, the system behavior is locally hardening but globally softening.

The proposed technique provides global behavior of the system near primary and secondary resonances. We confirmed that primary resonance of the first mode can lead to dynamic pull-in, as reported by Nayfeh et al. (2007). We also found the same dynamic pull-in

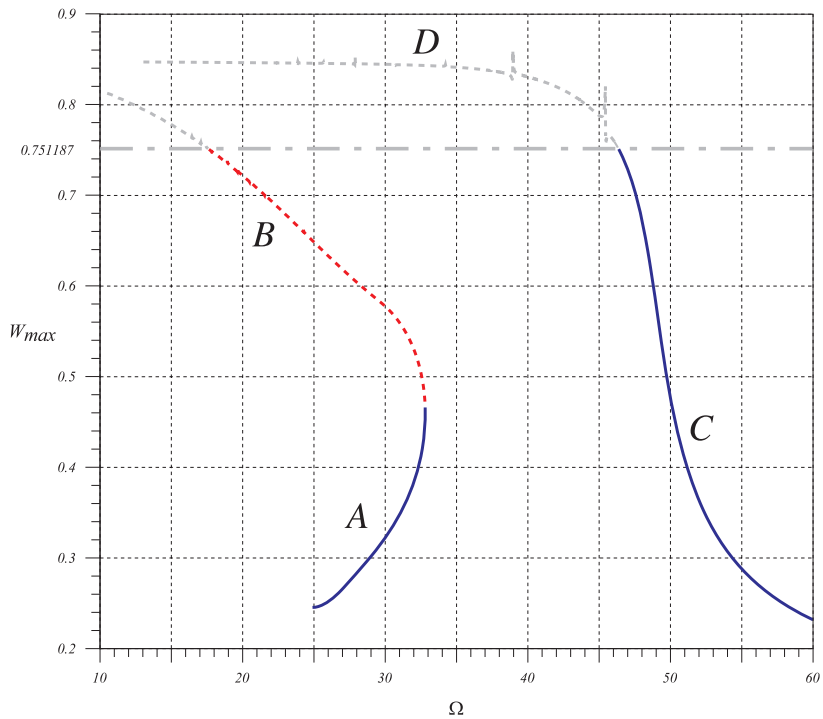

Figure 24. Frequency-response curve for the subharmonic resonance of order $\frac{1}{2}$ of the microactuator under loading Case 4.

phenomenon for secondary resonances of the first mode, for both locally hardening-type and softening-type resonators, when the level of the external excitation is sufficiently large. Increasing the DC voltage V_p and operating in the softening-type domain increases the possibility of, but is not a necessary condition for, dynamic pull-in due to superharmonic resonances. We identified simultaneous resonances or spikes associated with the first and third modes and those associated with the first and fourth modes. These spikes were found to be near the primary and secondary resonances for systems with either softening and local hardening behavior.

Floquet theory was used to ascertain the stability of the computed limit cycles at all points on the frequency-response curves. Its results were found to be sensitive to the accuracy of the computed limit cycle. Using 100 points in the FDM discretization yields smooth and accurate limit cycles whose stability can be ascertained using Floquet theory. On the other hand, for very large orbits, using 100 points in the FDM discretization yields nonsmooth and hence inaccurate limit cycles; consequently, their stability cannot be ascertained by Floquet theory. In the latter case, we used long-time integration to determine the local stability of large orbits. It was observed that, before pull-in occurs, the simulated large orbits with long-time integration were crossing the marginal stability line (representing the saddle) without having pull-in, which might be the result of either a shift in the saddle location due to the AC loading or a projection of the six-dimensional phase portrait on a two-dimensional plane. We

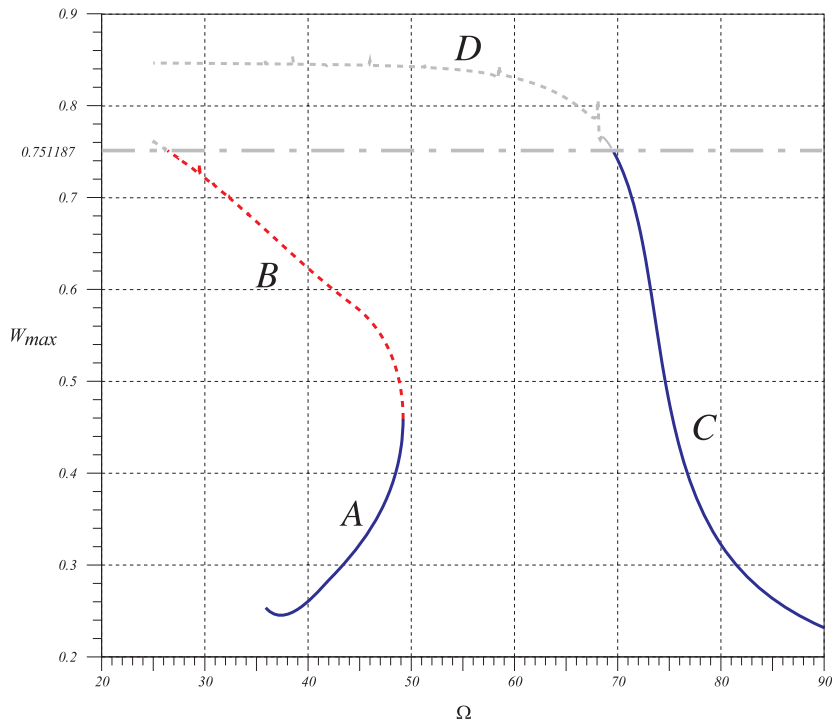

Figure 25. Frequency-response curve for the subharmonic resonance of order $\frac{1}{3}$ of the microactuator under loading Case 4.

note also that the stability results obtained with long-time integration depend on the initial conditions.

REFERENCES

Abdel-Rahman, E. M., Younis, M. I. and Nayfeh, A. H., 2005, "Finite-amplitude motions of beam resonators and their stability," *Journal of Computational and Theoretical Nanoscience* **1**, 1–7.

Bert, C. W. and Malik, M., 1996, "Differential quadrature method in computational mechanics: a review," *Applied Mechanics Review* **49**, 1–28.

Chao, P. C. P., Chiu, C. W. and Tsai, C. Y., 2006, "A novel method to predict the pull-in voltage in a closed form for micro-plates actuated by a distributed electrostatic force," *Journal of Micromechanics and Microengineering* **16**, 986–998.

De, S. K. and Aluru, N. R., 2006, "Complex nonlinear oscillations in electrostatically actuated microstructures," *Journal of Microelectromechnical Systems* **15**, 355–369.

Kuang, J. H. and Chen, C. J., 2004, "Dynamic characteristics of shaped micro-actuators solved using the differential quadrature method," *Journal of Micromechanics and Microengineering* **14**, 647–655.

Lenci, S. and Rega, G., 2006, "Control of pull-in dynamics in a nonlinear thermoelastic electrically actuated microbeam," *Journal of Micromechanics and Microengineering* **16**, 390–401.

Mehner, J. E., Gabbay, L. D. and Senturia, S. D., 2000, "Computer-aided generation of nonlinear reduced-order dynamic macromodels—II: Stress-stiffened case," *Journal of Micromechanics and Microengineering* **9**, 270–278.

Mukherjee, T., Fedder, G. K., Ramaswamy, D. and White, J., 2000, "Emerging simulation approaches for micromachined devices," *IEEE Transactions on Computer-aided Design of Integrated Circuits and Systems* **19**, 1572–1589.

Najar, F., Choura, S., Abdel-Rahman, E. M., El-Borgi, S. and Nayfeh, A. H., 2006, "Dynamic analysis of variable-geometry electrostatic microactuators," *Journal of Micromechanics and Microengineering* **16**, 2449–2457.

Najar, F., Choura, S., El-Borgi, S., Abdel-Rahman, E. M. and Nayfeh, A. H., 2005, "Modeling and design of variable-geometry electrostatic microactuators," *Journal of Micromechanics and Microengineering* **15**, 419–429.

Nayfeh, A. H. and Balachandran, B., 1995, *Applied Nonlinear Dynamics*, Wiley, New York.

Nayfeh, A. H. and Mook, D. T., 1979, *Nonlinear Oscillations*, Wiley, New York.

Nayfeh, A. H. and Younis, M. I., 2005, "Dynamics of MEMS resonators under superharmonic and subharmonic excitations," *Journal of Micromechanics and Microengineering* **15**, 1840–1847.

Nayfeh, A. H., Younis, M. I. and Abdel-Rahman, E. M., 2007, "Dynamic pull-in phenomenon in MEMS resonators," *Nonlinear Dynamics* **48**, 153–163.

Shkel, A. M., 2006, "Type I and Type II micromachined vibratory gyroscopes," in *Proceedings of the IEEE/Institute Of Navigation Plans*, San Diego, CA, April 25–27, pp. 586–593.

Veijola, T., Kuisma, H. and Lahdenperä, J., 1998, "Dynamic modelling and simulation of microelectromechanical devices with a circuit simulation program," in *Proceedings of the 1998 International Conference on Modeling and Simulation of Microsystems (MSM'98)*, Santa Clara, CA, April 6–8, pp. 245–250.

Younis, M. I., 2001, "Investigation of the mechanical behavior of microbeam-based MEMS devices," MSc Thesis, Virginia Polytechnic Institute and State University.

Younis, M. I., Abdel-Rahman, E. M. and Nayfeh, A. H., 2003, "A reduced-order model for electrically actuated microbeam-based MEMS," *Journal of Microelectromechnical Systems* **12**, 672–680.

Zook, J. D., Burns, D. W., Guckel, H., Sniegowski, J. J., Engelstad, R. L. and Feng, Z., 1992, "Characteristic of polysilicon resonant microbeam," *Sensors and Actuators A* **35**, 290–294.